



## Graphene-supported palladium phosphide PdP<sub>2</sub> nanocrystals for ethanol electrooxidation



Junfeng Liu<sup>a</sup>, Zhishan Luo<sup>a</sup>, Junshan Li<sup>a</sup>, Xiaoting Yu<sup>a</sup>, Jordi Llorca<sup>b</sup>, Déspina Nasiou<sup>c</sup>, Jordi Arbiol<sup>c,d</sup>, Michaela Meyns<sup>a,\*,1</sup>, Andreu Cabot<sup>a,d,\*</sup>

<sup>a</sup> Catalonia Institute for Energy Research (IREC), Sant Adrià de Besòs, 08930 Barcelona, Spain

<sup>b</sup> Institute of Energy Technologies, Department of Chemical Engineering and Barcelona Research Center in Multiscale Science and Engineering, Universitat Politècnica de Catalunya, Edvard Maristany 10-14, 08019, Barcelona, Spain

<sup>c</sup> Catalan Institute of Nanoscience and Nanotechnology (ICN2), CSIC and BIST, Campus UAB, Bellaterra, 08193, Catalonia, Spain

<sup>d</sup> ICREA, Pg. Lluís Companys 23, 08010, Barcelona, Catalonia, Spain

### ARTICLE INFO

**Keywords:**  
Palladium diphosphide  
Colloidal synthesis  
Electrocatalysis  
Ethanol oxidation

### ABSTRACT

We present a procedure to produce single-phase PdP<sub>2</sub> nanocrystals (NCs). The approach involves the reaction of palladium(II) acetylacetone and hexamethylphosphoroustriamide to nucleate defective Pd<sub>5</sub>P<sub>2</sub> nanoparticles that subsequently, with further phosphorous incorporation, crystallize into PdP<sub>2</sub>. The synthesized PdP<sub>2</sub> NCs were supported on reduced graphene oxide (rGO) and applied as electrocatalysts for ethanol oxidation. The activity of PdP<sub>2</sub> toward the ethanol oxidation reaction (EOR) was over a threefold higher than that of Pd NCs prepared under similar conditions. Even better performance was obtained from PdP<sub>2</sub> NCs supported on rGO, which showed current densities up to 51.4 mA cm<sup>-2</sup> and mass activities of 1.60 A mg<sup>-1</sup>Pd, that is 4.8 and 15 times higher than Pd NCs. Besides, PdP<sub>2</sub> NCs and PdP<sub>2</sub>/rGO catalysts showed improved stability during EOR than Pd NCs and Pd/rGO.

### 1. Introduction

Direct liquid fuel cells are electrochemical devices able to directly convert chemical energy stored within liquid fuels into electricity. Among the possible liquids, ethanol has a high energy density (8.01 KW h kg<sup>-1</sup>) [1,2], low toxicity, a relatively high boiling point for safe storage and transportation, and the potential to be bio-sourced in large quantities from the fermentation of biomass. Owing to these advantages, direct ethanol fuel cells (DEFCs) have become one of the most appealing alternatives to electrochemical batteries and conventional fossil fuel-based combustion engines in numerous fields of application. However, the high price and limited performance of current fuel oxidation electrocatalysts is limiting their deployment. These limitations, extensive to most fuel cell technologies, are particularly severe in DEFCs since the complete ethanol oxidation reaction (EOR) involves the release of 12 electrons per molecule and the cleavage of a C–C bond.

Extensive research on electrocatalysts for DEFCs has been carried out on acidic conditions, which allow taking advantage of convenient proton exchange membranes for the device fabrication. However, the

slow reaction kinetics and low stability of electrocatalysts in these conditions are very tough barriers to be overcome [3,4]. As an alternative, effort has been moved toward developing electrocatalysts for alkaline-type DEFCs. The enhanced kinetics of the catalytic reaction in alkaline solution increases the efficiency in the use of precious metals and even permits the use of less expensive catalysts.

Pt and Pt-based alloys have been extensively studied as the most active catalysts for DEFCs. Alternatively, Pd is a more abundant and less demanded element, what currently translates into significantly lower costs. Pd [5] and Pd-based electrocatalysts, such as PdNi [6,7], Pd<sub>2</sub>Ru [8], PdCu [9–11], PdAu [12] and Pd<sub>2</sub>Sn [4,13], have demonstrated electrocatalytic activities in the electrooxidation of different types of liquid fuels and particularly ethanol comparable to those of Pt-based catalysts. Pd and Pd-based materials are also excellent catalysts for the Suzuki coupling reaction [14–16] and oxygen reduction reaction [17]. An especially interesting case is that of Pd-based phosphides, which have shown excellent activity toward hydrogen evolution, oxygen reduction, formic acid oxidation and hydrodesulfurization [18,19]. Additionally, palladium phosphides are characterized with high electrical

\* Corresponding authors at: Catalonia Institute for Energy Research (IREC), Sant Adrià de Besòs, 08930 Barcelona, Spain

E-mail addresses: [michaela.meyns@awi.de](mailto:michaela.meyns@awi.de) (M. Meyns), [acabot@irec.cat](mailto:acabot@irec.cat) (A. Cabot).

<sup>1</sup> Current address: Alfred-Wegener-Institute, Helmholtz Centre for Polar and Marine Research, Biologische Anstalt Helgoland, Kurpromenade 201, 27498 Helgoland, Germany.

conductivities and show improved corrosion resistance with respect to Pd. However, surprisingly, palladium phosphides have not been investigated as electrocatalysts for the EOR.

Actually, few attempts have been done to produce palladium phosphide NCs at all. Most attempts to produce palladium phosphides were based on the reaction of premade Pd with a phosphorus precursor such as trioctylphosphine (TOP) or white phosphorous at relatively high temperatures [18,20–22]. Following this strategy, quasi amorphous palladium phosphide particles with irregular shapes and broad size distributions were obtained [21,22]. The synthesis of crystalline palladium phosphide NCs have proved to be very challenging. Single-phase Pd<sub>5</sub>P<sub>2</sub> crystallites with a few hundred nanometers were prepared using Pd(acac)<sub>2</sub> as metal precursor and TOP as phosphorus precursor [19]. Using the same strategy, Pd<sub>5</sub>P<sub>2</sub> nanoparticles encapsulated within mesoporous silica were also prepared [19].

Herein, we report a procedure to produce single-phase colloidal PdP<sub>2</sub> NCs. Compared with previous synthesis strategies based on the reaction of premade metallic Pd with a phosphorous source, our protocol involved the nucleation of Pd<sub>5</sub>P<sub>2</sub> and their subsequent crystallization and growth into PdP<sub>2</sub> NCs with the incorporation of additional P. After ligand exchange, PdP<sub>2</sub> NCs were uniformly deposited on reduced graphene oxide sheets and tested as electrocatalysts for the EOR.

## 2. Experimental

### 2.1. Chemicals

Hexamethylphosphoroustriamide (HMPT, 97%), and palladium(II) acetylacetone (Pd(acac)<sub>2</sub>, Pd 34.7 wt%) were purchased from Alfa Aesar. Oleylamine (OAm, approximate C18 content 80–90%) was purchased from ACROS Organics. TOP (97%), methylamine hydrochloride (MAHC, 98%), ammonium thiocyanate (NH<sub>4</sub>SCN, 99%), ammonium chloride (NH<sub>4</sub>Cl, 99.5%), potassium hydroxide (KOH, 85%), Nafion (5 wt% in a mixture of low aliphatic alcohols and water), graphite, potassium permanganate (KMnO<sub>4</sub>, 99%), sodium nitrate (NaNO<sub>3</sub>, 99%), sulfuric acid (H<sub>2</sub>SO<sub>4</sub>, 95–98%), hydrochloric acid (HCl, 37%), hydrogen peroxide (H<sub>2</sub>O<sub>2</sub>, 30 wt% in H<sub>2</sub>O) were obtained from Sigma-Aldrich. Chloroform, ethanol and acetone were of analytical grade and obtained from various sources. MilliQ water was obtained by using a PURELAB flex from ELGA. All chemicals were used as received without further purification.

### 2.2. Synthesis of PdP<sub>2</sub> NCs

Caution: Because this procedure involves the use and high-temperature decomposition of HMPT that can liberate toxic and flammable phosphine gas or toxic phosphorus oxides, the reaction should only be carried out by appropriately trained personnel using rigorously air-free conditions and the Schlenk line should be connected with gas absorption solutions.

In a typical synthesis, 60.9 mg (0.2 mmol) of Pd(acac)<sub>2</sub>, 67.5 mg (1 mmol) of MAHC or 53.5 mg (1 mmol) ammonium chloride, and 10 mL of OAm were mixed in a 50 mL three-neck flask. The reaction system was purged with argon at 120 °C for 1 h. Then 0.1 mL (0.57 mmol) of HMPT was injected into the solution and the temperature was further increased to 300 °C in 20 min. During the heating up, the solution became black at around 250 °C. The flask was maintained at 300 °C for 1 h before the solution was allowed to cool to room temperature. The isolation of the resultant black precipitate was achieved with excess ethanol followed by centrifugation at 5000 rpm (3200 g). Purification was achieved by multiple dispersion/precipitation steps using chloroform and ethanol. Finally the powder was suspended in 5 mL of chloroform in a vial.

### 2.3. Synthesis of Pd NCs

Reference Pd NCs were prepared in a similar way as PdP<sub>2</sub> NCs, i.e. by mixing the same amounts of Pd(acac)<sub>2</sub>, MAHC and OAm and at the same condition as in the synthesis of PdP<sub>2</sub> NCs, but without injection of HMPT. The reaction was kept at 300 °C for 1 h and then washed following the same procedures as in the synthesis of PdP<sub>2</sub> NCs.

### 2.4. Synthesis of rGO

Graphene oxide was produced by a modified Hummers method as originally presented by Kovtyukhova [23]. Briefly, in a 500 mL flask, 2.0 g of graphite, 1.5 g of NaNO<sub>3</sub> and 96 mL of concentrated H<sub>2</sub>SO<sub>4</sub> were vigorously stirred in ice-water bath. Then, 9.0 g of KMnO<sub>4</sub> was slowly added to the flask over 30 min. Stirring was continued for 1.5 h in the ice-water bath and then followed by another 2 h at 35 °C. Afterward, 280 mL of H<sub>2</sub>O was added into the mixture. During the process, the solution was heated to 98 °C and kept at this temperature for 2 h. 5 mL of 30 wt% H<sub>2</sub>O<sub>2</sub> were added to the solution after the temperature was decreased to 60 °C. To remove ionic impurities, the obtained solution was washed by vacuum filtration and rinsing with aqueous 3 wt% HCl for 3 times, followed by H<sub>2</sub>O for another 3 times. The resulting product was dried under vacuum at 60 °C and then calcined in a tube furnace at 500 °C for 2 h in flowing argon. As a result, the reduced graphene oxide (rGO) was obtained.

### 2.5. Ligand exchange

The ligand exchange procedure used here was similar to that previously reported by Fafarman et al. [24]. In a typical procedure, 0.5 mL of 130 mM NH<sub>4</sub>SCN in acetone was added to 1 mL of a dispersion of as-synthesized PdP<sub>2</sub> NCs in chloroform (~10 mg in 1 mL). The resulting solution was agitated for 1 min; a complete flocculation was observed within seconds. The slurry was centrifuged at 3000 rpm (1200 g) for 1 min and the supernatant discarded. Another 1 mL of acetone was added to the precipitate; the mixture was sonicated for 1 min followed by centrifuge at 3000 rpm for 1 min. The washing steps were repeated another time and the obtained precipitate was dried at room temperature.

### 2.6. Catalyst preparation

The catalyst ink for electrochemical measurements was prepared by mixing 5 mg of PdP<sub>2</sub> NCs and 5 mg of rGO in 5 mL of deionized water. The mixture was sonicated for 1 h to form a homogeneous catalyst ink. For comparison, catalysts of Pd, Pd/C, Pd/rGO and PdP<sub>2</sub> were also prepared through dissolving 10 mg of as-synthesized Pd, Pd and rGO (1:1 wt ratio) or PdP<sub>2</sub> NCs in 5 mL of deionized water by sonication for 1 h.

The working electrode was prepared using a glassy carbon electrode (GCE, 5 mm in diameter) which was previously polished using diamond paper and 0.05 µm alumina slurry sequentially, followed by ultrasonication in ethanol first and water later, for 1 min each. The cleaned GCE was dried under argon flow at room temperature. The electrode was modified by drop casting 10 µL of the catalyst ink and posterior drying at room temperature. To immobilize the catalysts on the electrode, 10 µL of a 0.5 wt% Nafion solution was dropped on the surface of the electrode.

### 2.7. Electrochemical measurements

Electrochemical measurements were conducted at room temperature on a BioLogic electrochemical workstation using a standard three-electrode cell with the modified GCE as working electrode, a Pt mesh as counter electrode and Hg/HgO (1 M KOH) as reference electrode. All the cyclic voltammetry (CV) measurements were conducted at room

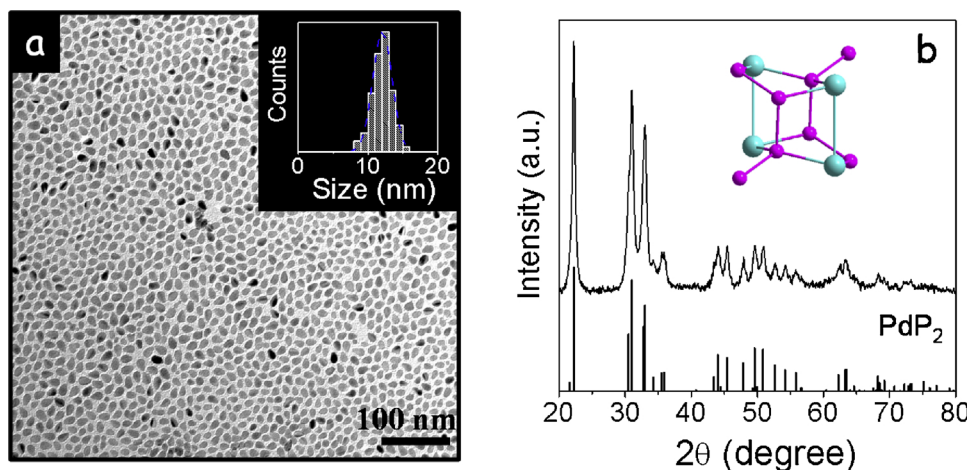


**Fig. 1.** a) Representative TEM micrograph of PdP<sub>2</sub> NCs. The inset shows their size (long axis) distribution histogram. b) XRD pattern of PdP<sub>2</sub> NCs including the JCPDS 77-1421 reference. The inset shows a unit cell of the PdP<sub>2</sub> monoclinic phase (Pd in blue and P in pink) (For interpretation of the references to colour in this figure legend, the reader is referred to the web version of this article).

temperature. The electrolyte solutions were purged with argon for 30 min before use. The background was obtained by CV measurement in 0.5 M KOH solution from −1.0 to 0.3 V vs. Hg/HgO at 50 mV s<sup>−1</sup>. Afterward, for EOR measurement, the working electrodes were tested in 0.5 M KOH with 0.5 M ethanol solution under the same conditions. The chronoamperometry measurements were conducted at −0.1 V vs. Hg/HgO for 10,000 s in the electrolyte of 0.5 M KOH and 0.5 M ethanol in order to evaluate the stability of the catalysts.

### 2.8. Characterization

Transmission electron microscopy (TEM) characterization was carried out using a ZEISS LIBRA 120, operating at 120 kV and a JEOL 1011 operating at 100 kV. Carbon-coated TEM grids from Ted-Pella were used as substrates. High-resolution TEM (HRTEM) studies were conducted using a field emission gun FEI™ Tecnai F20 microscope at 200 kV with a point-to-point resolution of 0.19 nm. Annular dark-field (HAADF) STEM was combined with electron energy loss spectroscopy (EELS) in the Tecnai F20, by using a GATAN QUANTUM filter. Scanning electron microscopy (SEM) analyses were done in a ZEISS Auriga microscope with an energy dispersive X-ray spectroscopy (EDS) detector operating at 20 kV. Powder X-ray diffraction (XRD) patterns were collected directly from the as-synthesized NCs dropped on Si (501) substrate on a Bruker-AXS D8 Advanced X-ray diffractometer with Ni-filtered (2 μm thickness) Cu K radiation ( $\lambda = 1.5406 \text{ \AA}$ ) operating at 40 kV and 40 mA. A LynxEye linear position-sensitive detector was used in reflection geometry. X-ray photoelectron spectroscopy (XPS) was done on a SPECS system equipped with an Al anode XR50 source operating at 150 mW and a Phoibos 150 MCD-9 detector. The pressure in the analysis chamber was below  $10^{-7} \text{ Pa}$ . The area analyzed was about  $2 \text{ mm} \times 2 \text{ mm}$ . The pass energy of the hemispherical analyzer was set at 25 eV and the energy step was set at 0.1 eV. Data processing was performed with the CasaXPS program (Casa Software Ltd., UK). Binding energy values were centered using the C 1 s peak at 284.8 eV. Fourier transform infrared spectroscopy (FTIR) was performed on an Alpha Bruker FTIR spectrometer with a platinum attenuated total reflectance (ATR) single reflection module. FTIR spectra data were recorded from  $400 \text{ cm}^{-1}$  to  $4000 \text{ cm}^{-1}$ .

## 3. Results and discussion

### 3.1. NC synthesis

PdP<sub>2</sub> NCs were produced within OAm from the reaction of Pd(acac)<sub>2</sub> with HMPT in the presence of MAHC (see details in the experimental section). All elements were introduced in the reaction flask at a low temperature and the mixture was heated up to 300 °C. During the

heating up process, the solution became black at around 250 °C, indicating the precursor reaction at this temperature.

Fig. 1a shows a TEM micrograph of the NCs obtained after 1 h reaction at 300 °C. NCs showed elongated, tear drop-like geometry and had an average size of its longer axis of  $12 \pm 2 \text{ nm}$ . XRD patterns showed the NCs to have a PdP<sub>2</sub> monoclinic phase, with I2/c space group (Fig. 1b). No additional XRD peak corresponding to secondary crystal phases was detected. HRTEM analysis confirmed the monoclinic phase of the NCs and allowed determining the lattice parameters:  $a = 6.207 \text{ \AA}$ ,  $b = 5.857 \text{ \AA}$  and  $c = 5.874 \text{ \AA}$  (Fig. 2a). Annular dark field scanning TEM (ADF-STEM) and STEM-EELS elemental composition maps revealed all NCs to contain Pd and P and to have both elements uniformly distributed throughout each NC (Fig. 2b). SEM-EDS analysis showed the NCs to have an atomic ratio of P/Pd = 2.0 (Figure S1).

To gain inside of the NC growth mechanism, aliquots were extracted at different reaction times. Spherical nanoparticles with a highly defective/disordered Pd<sub>5</sub>P<sub>2</sub> phase, as deduced from the XRD band at about  $2\theta = 40^\circ$ , and an average size of 7 nm were recovered from aliquots extracted after 1 min reaction at 300 °C (Figure S2 and S3). As the reaction time increased, additional P was progressively incorporated into the Pd<sub>5</sub>P<sub>2</sub> nanoparticles, which crystallized into elongated PdP<sub>2</sub> NCs (Figure S2 and S3).

To determine the role of MAHC in the synthesis, the reaction was performed in the absence of this compound. In these conditions, before adding the P precursor, the solution changed to black at 120 °C, during the heating up process. XRD analysis of the recovered solid showed that it consisted of Pd (Figure S4). We conclude that in the absence of MAHC, the Pd precursor is reduced by OAm at low temperature, resulting in the formation of Pd NCs. Once HMPT was injected in the solution containing the reduced Pd precursor, Pd NCs reacted with P to produce very small Pd-P nanoparticles, which after reaction at 300 °C for 1 h resulted in a mixture of small Pd<sub>5</sub>P<sub>2</sub> and PdP<sub>2</sub> NCs (Figure S5).

In the presence of 0.2 mmol of MAHC, the precursors reacted at higher temperature, about 250 °C, indicating that the presence of MAHC prevented the reduction of the Pd precursor by OAm. After reacting at 300 °C for 1 h, teardrop shaped PdP<sub>2</sub> NCs with some spherical Pd<sub>5</sub>P<sub>2</sub> particles were obtained. With larger amounts of MAHC, the shape of the NCs became uniform and less spherical Pd-P quasi-amorphous particles were observed in the products (Figure S6). This last point was followed by the decrease of the XRD band at about  $2\theta = 40^\circ$  assigned to a disordered/defective Pd<sub>5</sub>P<sub>2</sub> phase (Figure S7), which was observed to decrease with the amount of MAHC introduced. This band completely disappeared when 1 mmol MAHC was present in the reaction system. At this point, pure phase PdP<sub>2</sub> NCs were obtained.

To elucidate the role of chlorine and the amine group of MAHC, the synthesis was carried out in the presence of NH<sub>4</sub>Cl instead of MAHC. In these conditions, a similar reaction temperature with respect to the

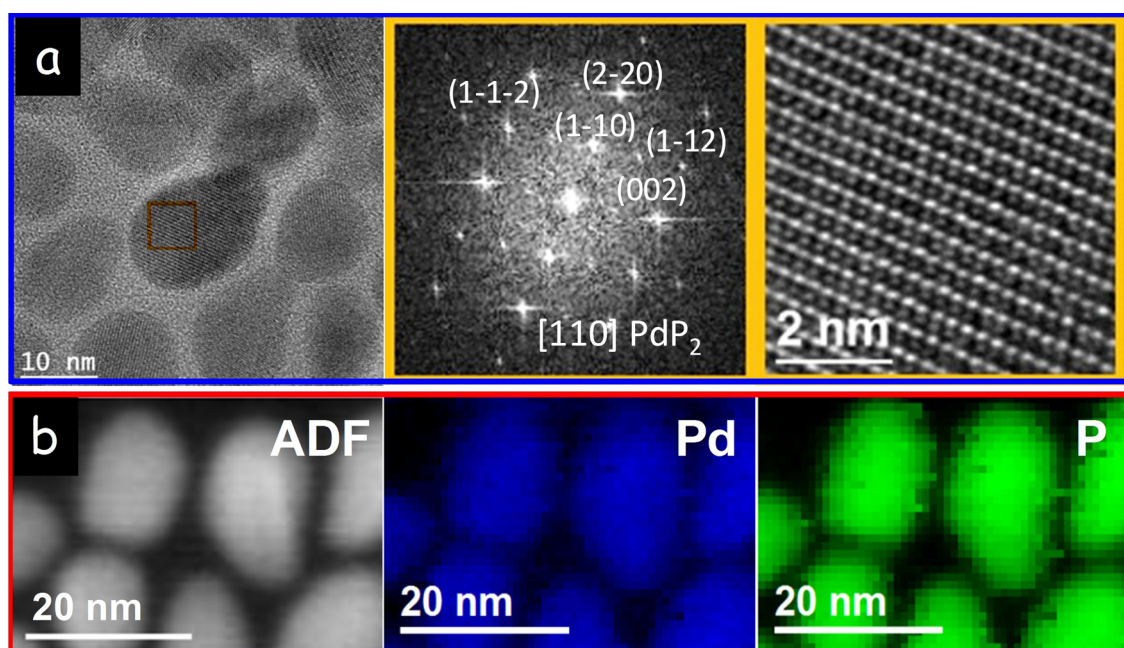


**Fig. 2.** a) HRTEM image of several PdP<sub>2</sub> NCs and power spectrum fitting with the PdP<sub>2</sub> phase of one of them. b) ADF-STEM image of several PdP<sub>2</sub> NCs and EELS compositional maps for Pd (blue) and P (green) (For interpretation of the references to colour in this figure legend, the reader is referred to the web version of this article).

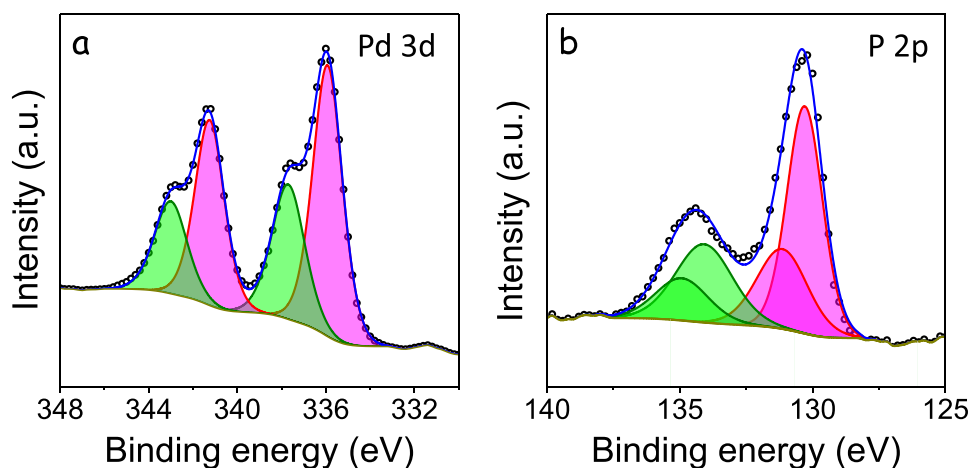


**Fig. 3.** XPS spectra of PdP<sub>2</sub> NCs in the Pd 3p (a) and P 2p (b) regions.

presence of MAHC, as observed from the color change of the solution, and a similar product was obtained (Figure S8). This experimental result pointed toward Cl<sup>-</sup> ions having a main role on the stabilization of the Pd precursor in solution, preventing its reduction with OAm and yielding pure phase PdP<sub>2</sub> when reacting with the P source. This result also demonstrates that ammonium chloride could be used instead of MAHC for the synthesis of PdP<sub>2</sub> NCs. However, all the following results were obtained using PdP<sub>2</sub> NCs produced in the presence of MAHC.

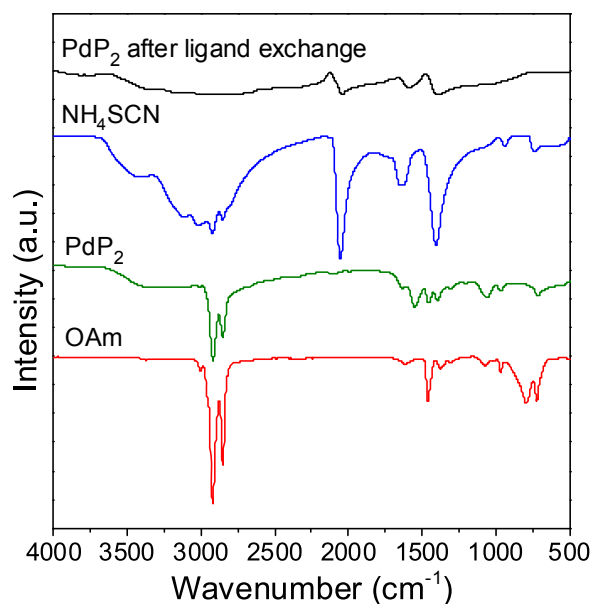
To determine the role of the P precursor, HMPT was replaced by TOP. Using TOP, no NCs were obtained at 300 °C, which we associated to the much lower reactivity of TOP when compared with HMPT. When reacting at 350 °C for 1 h, irregular and large-size NCs were produced (Figure S9). XRD and EDS showed these NCs to consist of a mixture of Pd<sub>5</sub>P<sub>2</sub> and PdP<sub>2</sub> phases (Figure S10). In this case, the produced NCs were irregular in shape and highly polydisperse in size.

Fig. 3 shows the Pd 3d and the P 2p XPS spectra of the PdP<sub>2</sub> NCs. Two doublets were fitted to the Pd 3d states. The main Pd component, accounting for 64% of the total Pd detected, was found at a Pd 3d<sub>5/2</sub>

binding energy 335.9 eV. This binding energy was slightly above that of Pd(0) in pure Pd (335.1–335.5 eV) [25,26], which is consistent with the chemical environment of Pd within a Pd phosphide. A more oxidized component, accounting for 36% of the Pd detected, was found at a Pd 3d<sub>5/2</sub> binding energy of 337.7 eV. This component was assigned to Pd (II) species at the surface of the air-exposed NCs that had undergone oxidation [27].

Two P chemical states were also identified from XPS analysis of the P 2p electronic states. A main P 2p<sub>3/2</sub> peak at 130.3 eV matched well with P in a metal phosphide environment. This component accounted for 64% of the detected P. The second component, accounting for 36% of the P detected, was found at a higher binding energy, P 2p<sub>3/2</sub> peak at 134.1 eV, and it was assigned to a phosphate environment. We believe this phosphate to result from the partial oxidation of the PdP<sub>2</sub> surface due to air exposure [28–30].

The atomic ratio of Pd and P at the NC surface detected by XPS was approximately 1, which points toward a Pd enriched surface compared to the PdP<sub>2</sub> core.



**Fig. 4.** FTIR of OAm,  $\text{NH}_4\text{SCN}$ , as-synthesized  $\text{PdP}_2$  NCs and  $\text{PdP}_2$  after ligand exchange by  $\text{NH}_4\text{SCN}$ .

### 3.2. NC surface treatment and catalyst preparation

FTIR spectra of as-produced  $\text{PdP}_2$  NCs displayed peaks at 2920 and  $2852 \text{ cm}^{-1}$  attributed to the C–H stretching vibration of the alkyl group of OAm (Fig. 4). Additionally, peaks attributed to the bending vibration of C–H in alkyl and alkenyl part of OAm, at  $1457$  and  $968 \text{ cm}^{-1}$ , and to the bending vibrations of N–H and C–N, at  $1551$  and  $1059 \text{ cm}^{-1}$ , were also identified. These features were slightly shifted compared with pure OAm, consistently with its binding to the NC surface. While the presence of OAm at the NC surface rendered the NCs colloidally stable in non-polar solvents and limited their growth, OAm might also block catalytic sites and hinder charge transfer. Thus, it had to be removed prior to NC catalytic application.

OAm was displaced from the NC surface using a short inorganic ligand, ammonium thiocyanate, following the procedure reported by Fafarman et al. (see experimental section for details) [24]. FTIR spectra of the NCs after ligand displacement with ammonium thiocyanate showed the presence of peaks at  $2045$  and  $1596 \text{ cm}^{-1}$ , assigned to the  $\text{C}\equiv\text{N}$  antisymmetric and asymmetric vibration, and a broad peak at ca.  $1400 \text{ cm}^{-1}$  corresponding to the N–H stretching vibration of the amino group of ammonium thiocyanate ( $\text{NH}_4\text{SCN}$ ).

Electrocatalysts were prepared by supporting the colloidal  $\text{PdP}_2$  NCs onto reduced graphene oxide (rGO). Graphene is considered an ideal electrocatalyst support owing to its excellent electric conductivity, large surface area, superior mechanical flexibility and chemical stability [31]. The use of graphene as the support material not only improves the electrical conductivity of the nanocomposite catalyst, but also increases the dispersion of the active components, which helps to prevent their aggregation during the catalytic reaction. Graphene oxide (GO) sheets were prepared here by a modified Hummers method as presented by Kovtyukhova [23], and then reduced to rGO at high temperature (Figure S11). rGO exhibited a rippled and crumpled morphology and paper-like structure with single or few layers (Fig. 5), offering a large surface area to support the  $\text{PdP}_2$  NCs.  $\text{PdP}_2$  NCs were supported by mixing the proper amount of rGO and  $\text{PdP}_2$  NCs in water (see experimental section for details). As shown in Fig. 5,  $\text{PdP}_2$  NCs were homogeneously distributed on the rGO sheet after solvent removal. The nanocomposite was drop-casted onto GCE and then dried at room temperature. On top of it, Nafion was deposited to immobilize the catalysts on the electrode (see details in the experimental section).

### 3.3. Cyclic voltammetry in base solution

CV of  $\text{PdP}_2/\text{rGO}$ , unsupported  $\text{PdP}_2$ ,  $12 \pm 3 \text{ nm}$  Pd (Figure S12) and  $\text{Pd}/\text{rGO}$  electrocatalysts was initially investigated in a  $0.5 \text{ M KOH}$  aqueous solution (Fig. 6a). The same total amount of catalyst was used to produce each of the tested electrodes, which translated into significantly lower amounts of Pd in the  $\text{PdP}_2$  and especially on the  $\text{PdP}_2/\text{rGO}$  catalysts.

All catalysts showed similar coulombic features, but with small differences in relevant regions of the voltammograms. The peaks in the region between  $-0.6 \text{ V}$  and  $-0.8 \text{ V}$  vs.  $\text{Hg/HgO}$  were attributed to the adsorption (cathodic scan) and desorption (anodic scan) of hydrogen. In the anodic scan, the  $\text{PdP}_2$  catalyst showed a positive shift of peak potentials compared to Pd, while in the cathodic scan, the  $\text{PdP}_2$  showed a slight negative shift of the peak potential. The distinct anodic and cathodic behaviors of  $\text{PdP}_2$  and Pd catalysts were related to their different electronic structure involving partial electron donation from Pd to P sites, consistent with XPS results [32].

The peaks in the anodic scan region from  $-0.4$  to  $-0.2 \text{ V}$  vs.  $\text{Hg/HgO}$  were attributed to the formation of palladium oxide on the NC surface. Subsequently, a  $\text{PdO}$  reduction peak appeared at about  $-0.2 \text{ V}$  vs.  $\text{Hg/HgO}$  during the negative scans. The electrochemically active surface area (ECSA) of the catalysts was estimated from the coulombic charge for the reduction of  $\text{PdO}$ , i.e. from the area over the voltammetry curve in the  $\text{PdO}$  reduction peak region [13]:

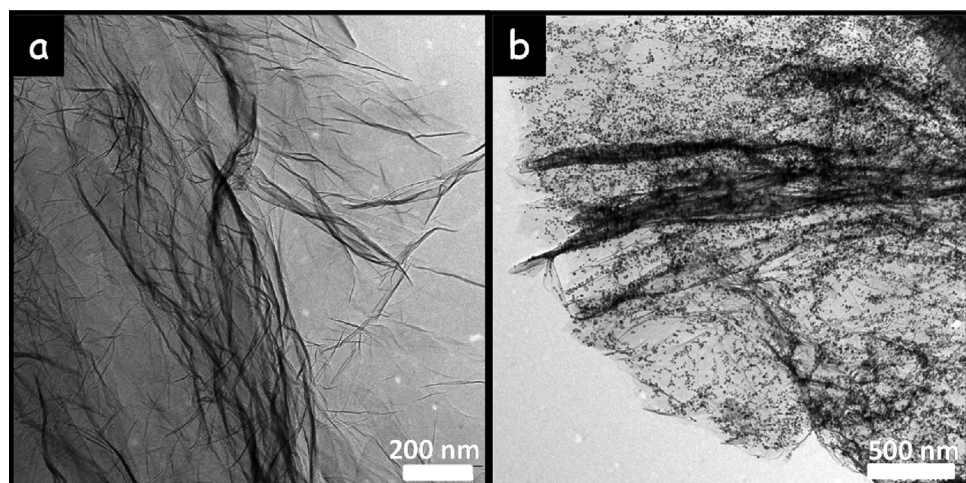


**Fig. 5.** TEM images of as-prepared rGO (a) and  $\text{PdP}_2/\text{rGO}$  (b) catalyst.

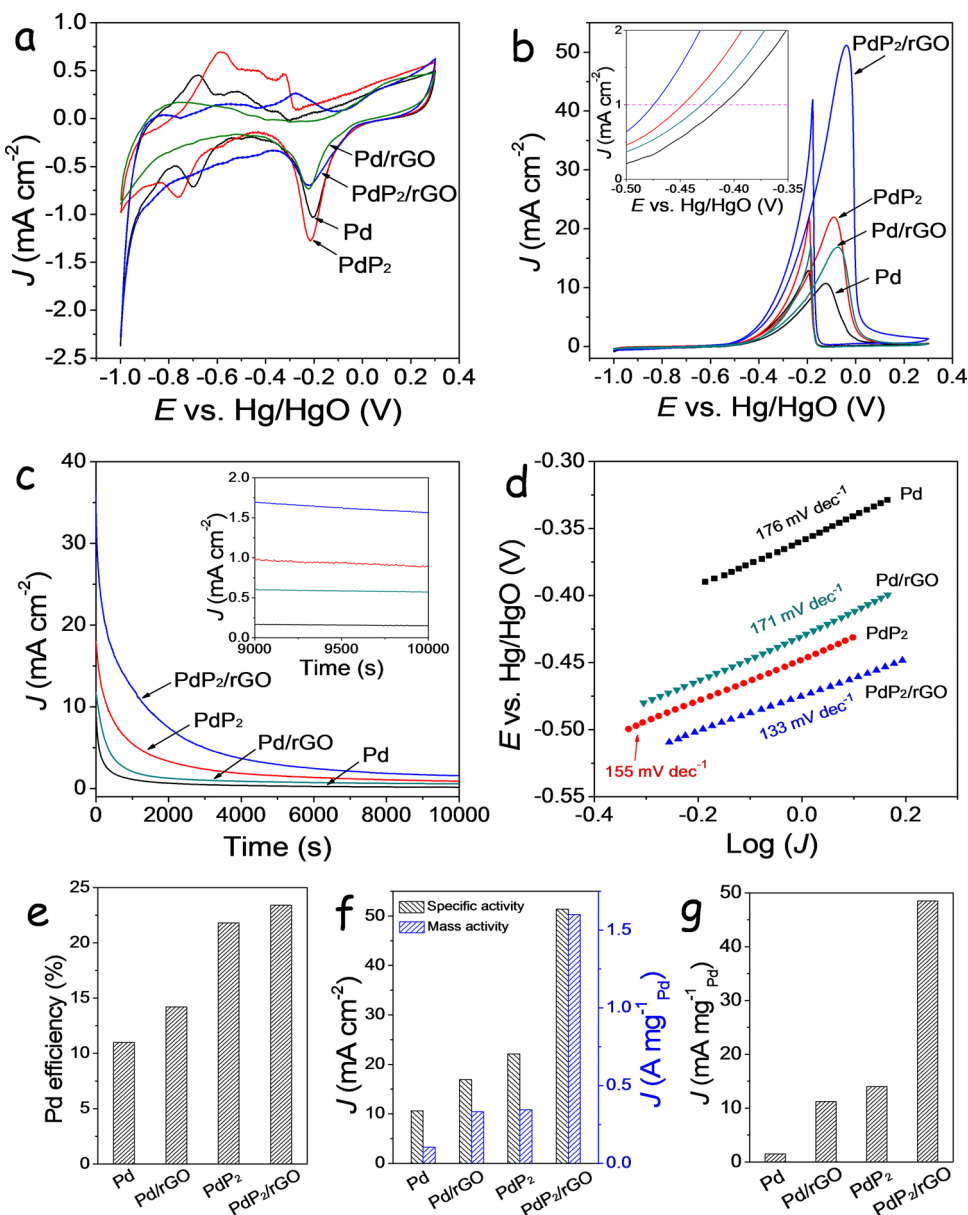


**Fig. 6.** a) Cyclic voltammetry measurements of Pd, Pd/rGO, PdP<sub>2</sub> and PdP<sub>2</sub>/rGO in a 0.5 M KOH solution and b) in a 0.5 M KOH + 0.5 M ethanol solution. c) Chronoamperometric measurements of Pd, Pd/rGO, PdP<sub>2</sub> and PdP<sub>2</sub>/rGO in a 0.5 M KOH + 0.5 M ethanol solution at -0.1 V vs.  $\text{Hg/HgO}$ . d) Tafel plot of the Pd, Pd/rGO, PdP<sub>2</sub> and PdP<sub>2</sub>/rGO. e) Comparison of Pd utilization efficiencies. f) Comparison of specific activity and mass activity of the Pd, Pd/rGO, PdP<sub>2</sub> and PdP<sub>2</sub>/rGO. g) Mass activity after chronoamperometric measurement for 10,000 s.

$$\text{ECSA} = \frac{Q(\mu\text{C} \cdot \text{cm}^{-2})}{Q_{\text{PdO}}(\mu\text{C} \cdot \text{cm}^{-2}) \times \text{Pd}_{\text{loading}}(\text{mg} \cdot \text{cm}^{-2})} \times 10 \quad (1)$$

where  $Q_{\text{PdO}} = 405 \mu\text{C cm}^{-2}$  is the charge value given for the reduction of a PdO monolayer, the coulombic charge  $Q$  is calculated by integrating the area of the PdO reduction peak, and  $\text{Pd}_{\text{loading}}$  is the Pd mass on the working electrode.

ECSA values obtained for Pd, Pd/rGO, PdP<sub>2</sub>, and PdP<sub>2</sub>/rGO catalysts were  $49.4 \text{ m}^2 \text{ g}^{-1}$ ,  $63.8 \text{ m}^2 \text{ g}^{-1}$ ,  $97.9 \text{ m}^2 \text{ g}^{-1}$ , and  $105.1 \text{ m}^2 \text{ g}^{-1}$ , respectively. The Pd utilization effectiveness was estimated taking into account that the active surface area for full utilization of 1 g of Pd would be  $448 \text{ m}^2$  [13,33]. Thus, the Pd utilization efficiencies of PdP<sub>2</sub>, PdP<sub>2</sub>/rGO, Pd/rGO and Pd were 21.8%, 23.4%, 14.2% and 11.0%, respectively (Fig. 6e).

Besides slight differences related to the dissimilar geometry and size of PdP<sub>2</sub> and Pd NCs, the larger ECSA and Pd utilization efficiency of PdP<sub>2</sub> over Pd demonstrated PdP<sub>2</sub> to have a highly Pd-rich surface, as

observed from XPS measurements. The oxidation of PdP<sub>2</sub> beyond the surface monolayer could also partially explain the higher ECSA obtained for PdP<sub>2</sub>. Besides, the slightly improved Pd utilization efficiency of PdP<sub>2</sub>/rGO over unsupported PdP<sub>2</sub> might be attributed to the high surface area of rGO which allowed a better dispersion of the PdP<sub>2</sub> NCs.

#### 3.4. Cyclic voltammetry in ethanol solution

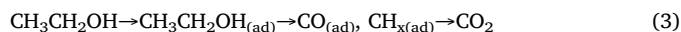
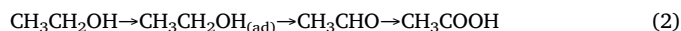
The EOR electrocatalytic activities of Pd, Pd/rGO, PdP<sub>2</sub> and PdP<sub>2</sub>/rGO catalysts were investigated in a 0.5 M KOH and 0.5 M ethanol aqueous solution (Fig. 6b). CVs from all catalysts showed the two well defined anodic peaks associated with the ethanol oxidation in alkaline media, one in the forward and one in the reverse scan. The oxidation peak in the forward scan was associated with the oxidation of freshly chemisorbed species coming from ethanol adsorption. The oxidation peak in the reverse scan was related to the removal of carbonaceous species that were not completely oxidized in the forward scan.

**Table 1**

Current density and potential at the forward and reverse peak and ratio of the peak current density between the forward and reverse oxidation peaks  $J_F/J_R$ .

Catalysts	Forward Scan		Reverse Scan		$J_F/J_R$
	$E_F$ (V vs. Hg/HgO)	$J_F$ ( $\text{mA cm}^{-2}$ )	$E_R$ (V vs. Hg/HgO)	$J_R$ ( $\text{mA cm}^{-2}$ )	
Pd	−0.12	10.6	−0.194	12.9	0.82
Pd/rGO	−0.07	16.9	−0.185	16.9	1.00
PdP <sub>2</sub>	−0.09	22.1	−0.192	22.3	0.99
PdP <sub>2</sub> /rGO	−0.04	51.4	−0.178	42.1	1.22

The ethanol oxidation process may take place through two parallel pathways [8]:



In the path schematized in equation 2 (C2 pathway), ethanol is first oxidized to acetaldehyde and subsequently to acetic acid or acetate in alkaline solution. The C–C bond is not broken during this pathway. In the path of equation 3 (C1 pathway), the C–C bond is broken and intermediate species such as CO and CH<sub>x</sub> fragments are produced, which can be further oxidized to CO<sub>2</sub> or carbonate in alkaline solution.

During the positive scan, to reach a current density of 1 mA cm<sup>−2</sup>, overpotentials of −0.48 V and −0.45 V vs. Hg/HgO were required for PdP<sub>2</sub>/rGO and PdP<sub>2</sub>, respectively, which was less than the overpotential required for Pd/rGO (−0.43 V vs. Hg/HgO) and Pd NCs (−0.41 V vs. Hg/HgO), indicating a lower activation energy for ethanol oxidation on PdP<sub>2</sub>. The forward oxidation current peaked at around −0.12 V vs. Hg/HgO for Pd, −0.09 V for PdP<sub>2</sub>, −0.07 V for Pd/rGO and −0.04 V for PdP<sub>2</sub>/rGO (Table 1). Higher potentials resulted in a decrease of current density associated with the oxidation of the Pd surface. In the forward scan, peak current densities for the EOR in Pd, Pd/rGO, PdP<sub>2</sub> and PdP<sub>2</sub>/rGO were 10.6, 16.9, 22.1 and 51.4 mA cm<sup>−2</sup>, respectively (Table 1). When the values were normalized to reflect the amount of Pd, the mass peak current density of PdP<sub>2</sub> and PdP<sub>2</sub>/rGO were 0.344 and 1.60 A mg<sup>−1</sup><sub>Pd</sub>, respectively, which is ca. 3.3 and 15 times higher than that of Pd (0.104 A mg<sup>−1</sup><sub>Pd</sub>), and 1.03 and 4.8 times higher than that of Pd/rGO (0.332 A mg<sup>−1</sup><sub>Pd</sub>) (Fig. 6f). Overall, PdP<sub>2</sub>/rGO showed very high specific and mass activities toward the EOR, comparable to the best Pt- and Pd-based catalysts reported to date (Fig. 7).

In terms of loading, while bare rGO showed no activity toward EOR (Figure S13), with the increasing amount of PdP<sub>2</sub> on rGO from 25% to 75%, the catalyst showed increasing specific activity and decreasing mass activity. A 50 wt% loading of PdP<sub>2</sub> on PdP<sub>2</sub>/rGO was considered the best compromise and was the composition selected to carry on all measurements.

The ratio of the forward ( $J_F$ ) and reverse ( $J_R$ ) peak current densities was calculated to get insight of the reaction pathway: the higher the  $J_F/J_R$  ratio, the more efficient is the oxidation of ethanol and the less accumulation of carbonaceous species occurs on the catalyst [4]. As calculated from Fig. 6b, the  $J_F/J_R$  ratios for Pd, Pd/rGO, PdP<sub>2</sub> and PdP<sub>2</sub>/rGO were 0.82 and 1.00 to 0.99 and 1.22, respectively (Table 1). The increased ratio suggested more efficient ethanol oxidation process for PdP<sub>2</sub> and especially PdP<sub>2</sub>/rGO than Pd.

To evaluate the stability of the catalysts, chronoamperometry (CA) measurements were carried out in a solution of 0.5 M KOH + 0.5 M ethanol with a constant applied potential of −0.1 V vs. Hg/HgO. As displayed in Fig. 6c, initial rapid decreases in current density were observed for all the catalysts, followed by a sluggish decrease until a pseudo-steady state. The sharp initial decrease was ascribed to the adsorption and accumulation of strongly adsorbed reaction intermediates on the surface of free active sites. Subsequently, the adsorption of ethanol depends on the liberation of the active sites resulting from the oxidation of ethanol or the intermediates that form during the

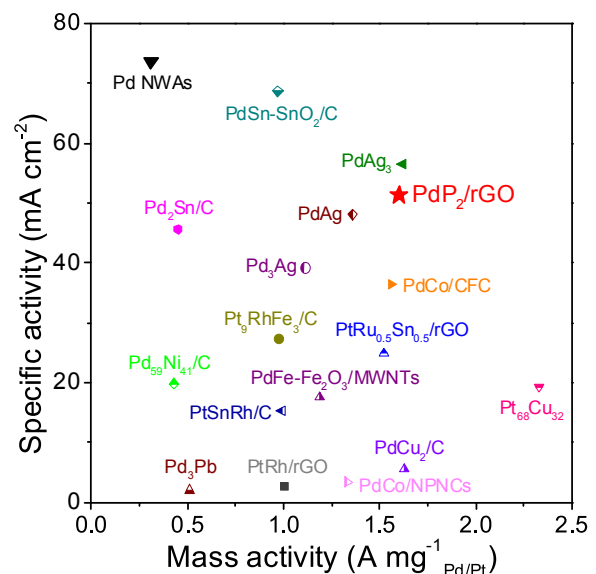


**Fig. 7.** Specific and mass activities of the PdP<sub>2</sub>/rGO electrocatalysts tested in the present work compared with reported best performing catalysts: PtRh/rGO [34], Pt<sub>9</sub>RhFe<sub>3</sub>/C [35], PtRu<sub>0.5</sub>Sn<sub>0.5</sub> [36], Pd<sub>2</sub>Sn/C [4], Pd<sub>59</sub>Ni<sub>41</sub>/C [37], Pd<sub>3</sub>Pb [38], PdCo/NPNCs [39], PdCu<sub>2</sub>/C [40], PdFe-Fe<sub>2</sub>O<sub>3</sub>/MWNTs [41], Pt<sub>68</sub>Cu<sub>32</sub> [42], Pd NWAs [43], PtCo/CFC [44], PdAg<sub>3</sub>, PdAg and Pd<sub>3</sub>Ag [45], PtCu [46], PtSnRh/C [47] and PdSn-SnO<sub>2</sub>/C [48]. Abbreviations: reduced graphene oxide (rGO), N-doped porous carbon nanocapsules (NPNCs), multiwalled carbon nanotubes (MWNTs), nanowire arrays (NWAs) and carbon fiber cloth (CFC).

initial state. After 10,000 s activity, the current obtained from PdP<sub>2</sub> (0.90 mA cm<sup>−2</sup>) and PdP<sub>2</sub>/rGO (1.56 mA cm<sup>−2</sup>) was much higher than that of Pd (0.15 mA cm<sup>−2</sup>) and Pd/rGO (0.57 mA cm<sup>−2</sup>). When comparing by mass activities, PdP<sub>2</sub>/rGO (48.5 mA mg<sup>−1</sup><sub>Pd</sub>) and PdP<sub>2</sub> (14.0 mA mg<sup>−1</sup><sub>Pd</sub>) showed about 32 and 9.5 times higher values than Pd (1.47 mA mg<sup>−1</sup><sub>Pd</sub>), and 4.3 and 1.3 times higher values than Pd/rGO (Fig. 6g). Notice that no morphological or structural change of the NCs was observed to take place during EOR (Figure S14).

Fig. 6d shows a linear region of the Tafel plots obtained from the CV curves in the range from −0.5 to −0.3 V vs. Hg/HgO. As the potential further increased above −0.2 V, the Tafel plot became curved, indicating a change in the factor limiting the reaction rate. As shown in Fig. 6d, Pd NCs and Pd/rGO showed a Tafel slope of 176 and 171 mV dec<sup>−1</sup>, well above that of PdP<sub>2</sub> and PdP<sub>2</sub>/rGO, with Tafel slopes of 155 and 133 mV dec<sup>−1</sup>, respectively. These values were close to the theoretical value for the EOR as calculated by Liang (120 mV dec<sup>−1</sup>) [49]. The lower Tafel slopes indicated that the charge-transfer kinetics of the EOR on the PdP<sub>2</sub> and especially PdP<sub>2</sub>/rGO catalysts were faster than that on Pd in the alkaline medium, which can be ascribed to the positive effect of P on the electronic state of Pd, the enhanced electron conductivity of rGO and the uniform dispersion of PdP<sub>2</sub> NCs on rGO.

#### 4. Conclusions

In summary, single-phase PdP<sub>2</sub> NCs were produced in the presence of chlorine ions and using a highly active P precursor, HMPT. PdP<sub>2</sub> NCs showed high mass activity and long-term stability toward the EOR in alkaline media. The enhanced properties were attributed to the effect of P on the electronic structure of Pd and the Pd-rich surface of the produced PdP<sub>2</sub> NCs. The activity and stability of the PdP<sub>2</sub>-based catalyst were further improved by supporting PdP<sub>2</sub> NCs onto rGO, taking advantage of an enhanced electrical conductivity and a high dispersion of the PdP<sub>2</sub> NCs. Additionally, the slower current decay over time combined with the higher measured activity for PdP<sub>2</sub> and PdP<sub>2</sub>/rGO electrocatalysts when compared with Pd and Pd/rGO, indicated a higher tolerance to the carbonaceous species formed.

## Notes

The authors declare no competing financial interest.

## Acknowledgements

This work was supported by the European Regional Development Funds and the Spanish MINECO project SEHTOP (ENE2016-77798-C4-3-R). D. Nasiou and J. Arbiol acknowledge funding from Generalitat de Catalunya 2017 SGR 327 and the Spanish MINECO project ANAPHASE (ENE2017-85087-C3). ICN2 acknowledges support from the Severo Ochoa Programme (SEV-2013-0295) and is funded by the CERCA Programme / Generalitat de Catalunya. J. Llorca is a Serra Hunter Fellow and is grateful to ICREA Academia program and grants MINECO/FEDER ENE2015-63969-R and GC 2017 SGR 128. J. Liu, J. Li and X. Yu thank the China Scholarship Council for scholarship support. M. Meyns acknowledges a Juan de la Cierva formación grant by the Spanish MINECO.

## Appendix A. Supplementary data

Supplementary material related to this article can be found, in the online version, at doi:<https://doi.org/10.1016/j.apcatb.2018.09.105>.

## References

- [1] S.T. Nguyen, H.M. Law, H.T. Nguyen, N. Kristian, S. Wang, S.H. Chan, X. Wang, Enhancement effect of Ag for Pd/C towards the ethanol electro-oxidation in alkaline media, *Appl. Catal. B Environ.* 91 (2009) 507–515.
- [2] W. Hong, J. Wang, E. Wang, Facile synthesis of highly active PdAu nanowire networks as self-supported electrocatalyst for ethanol electrooxidation, *ACS Appl. Mater. Interface* 6 (2014) 9481–9487.
- [3] M.D. Obradovic, Z.M. Stancic, U.C. Lacnjevac, V.V. Radmilovic, A. Gavrilovic-Wohlmuther, V.R. Radmilovic, S.L. Gojkovic, Electrochemical oxidation of ethanol on palladium-nickel nanocatalyst in alkaline media, *Appl. Catal. B Environ.* 189 (2016) 110–118.
- [4] Z. Luo, J. Lu, C. Flox, R. Nafria, A. Genç, J. Arbiol, J. Llorca, M. Ibáñez, J.R. Morante, A. Cabot, Pd<sub>2</sub>Sn [010] nanorods as a highly active and stable ethanol oxidation catalyst, *J. Mater. Chem. A* 4 (2016) 16706–16713.
- [5] Z. Zhang, Y. Dong, L. Wang, S. Wang, Scalable synthesis of a Pd nanoparticle loaded hierarchically porous graphene network through multiple synergistic interactions, *Chem. Commun.* 51 (2015) 8357–8360.
- [6] Z. Chen, J. Zhang, Y. Zhang, Y. Liu, X. Han, C. Zhong, W. Hu, Y. Deng, NiO-induced synthesis of PdNi bimetallic hollow nanocrystals with enhanced electrocatalytic activities toward ethanol and formic acid oxidation, *Nano Energy* 42 (2017) 353–362.
- [7] B. Cai, D. Wen, W. Liu, A.K. Herrmann, A. Benad, A. Eychmuller, Function-led design of aerogels: self-assembly of alloyed PdNi hollow nanospheres for efficient electrocatalysis, *Angew. Chem. Int. Ed.* 54 (2015) 13101–13105.
- [8] J. Guo, R. Chen, F.C. Zhu, S.G. Sun, H.M. Villalas, New understandings of ethanol oxidation reaction mechanism on Pd/C and Pd<sub>2</sub>Ru/C catalysts in alkaline direct ethanol fuel cells, *Appl. Catal. B Environ.* 224 (2018) 602–611.
- [9] K. Jiang, P. Wang, S. Guo, X. Zhang, X. Shen, G. Lu, D. Su, X. Huang, Ordered PdCu-based nanoparticles as bifunctional oxygen-reduction and ethanol-oxidation electrocatalysts, *Angew. Chem. Int. Ed.* 55 (2016) 9030–9035.
- [10] X. Zhao, L. Dai, Q. Qin, F. Pei, C. Hu, N. Zheng, Self-supported 3D PdCu alloy nanosheets as a bifunctional catalyst for electrochemical reforming of ethanol, *Small* 13 (2017) 1602970.
- [11] A. Serov, T. Asset, M. Padilla, I. Matanovic, U. Martinez, A. Roy, K. Artyushkova, M. Chatenet, F. Maillard, D. Bayer, C. Cremers, P. Atanassov, Highly-active Pd–Cu electrocatalysts for oxidation of ubiquitous oxygenated fuels, *Appl. Catal. B Environ.* 191 (2016) 76–85.
- [12] J. Liu, Y. Zheng, Z. Hong, K. Cai, F. Zhao, H. Han, Microbial synthesis of highly dispersed PdAu alloy for enhanced electrocatalysis, *Sci. Adv.* 2 (2016) e1600858.
- [13] C. Wang, Y. Wu, X. Wang, L. Zou, Z. Zou, H. Yang, Low temperature and surfactant-free synthesis of Pd<sub>2</sub>Sn intermetallic nanoparticles for ethanol electro-oxidation, *Electrochim. Acta* 220 (2016) 628–634.
- [14] J. Xi, H. Sun, D. Wang, Z. Zhang, X. Duan, J. Xiao, F. Xiao, L. Liu, S. Wang, Confined-interface-directed synthesis of Palladium single-atom catalysts on graphene/amorphous carbon, *Appl. Catal. B Environ.* 225 (2018) 291–297.
- [15] J. Liu, J. Hao, C. Hu, B. He, J. Xi, J. Xiao, S. Wang, Z. Bai, Palladium nanoparticles anchored on amine-functionalized silica nanotubes as a highly effective catalyst, *J. Phys. Chem. C* 122 (2018) 2696–2703.
- [16] X. Duan, J. Liu, J. Hao, L. Wu, B. He, Y. Qiu, J. Zhang, Z. He, J. Xi, S. Wang, Magnetically recyclable nanocatalyst with synergistic catalytic effect and its application for 4-nitrophenol reduction and Suzuki coupling reactions, *Carbon* 130 (2018) 806–813.
- [17] L. Bu, Q. Shao, Y. Pi, J. Yao, M. Luo, J. Lang, S. Hwang, H. Xin, B. Huang, J. Guo, D. Su, S. Guo, X. Huang, Coupled s-p-d exchange in facet-controlled Pd<sub>3</sub>Pb tripods enhances oxygen reduction catalysis, *Chemistry* 4 (2018) 359–371.
- [18] A.R.J. Kucernak, K.F. Fahy, V.N.N. Sundaram, Facile synthesis of palladium phosphide electrocatalysts and their activity for the hydrogen oxidation, hydrogen evolution, oxygen reduction and formic acid oxidation reactions, *Catal. Today* 262 (2016) 48–56.
- [19] G.H. Layan Savithra, R.H. Bowker, B.A. Carrillo, M.E. Bussell, S.L. Brock, Mesoporous matrix encapsulation for the synthesis of monodisperse Pd<sub>5</sub>P<sub>2</sub> nanoparticle hydrodesulfurization catalysts, *ACS Appl. Mater. Interface* 5 (2013) 5403–5407.
- [20] A.E. Henkes, Y. Vasquez, R.R. Schaak, Converting metals into phosphides: a general strategy for the synthesis of metal phosphide nanocrystals, *J. Am. Chem. Soc.* 129 (2007) 1896–1897.
- [21] S. Carenco, Y. Hu, I. Florea, O. Ersen, C. Boissiere, C. Sanchez, N. Mezailles, Structural transitions at the nanoscale: the example of palladium phosphides synthesized from white phosphorus, *Dalton Trans.* 42 (2013) 12667–12674.
- [22] S. Carenco, Y. Hu, I. Florea, O. Ersen, C. Boissiere, N. Mezailles, C. Sanchez, Metal-dependent interplay between crystallization and phosphorus diffusion during the synthesis of metal phosphide nanoparticles, *Chem. Mater.* 24 (2012) 4134–4145.
- [23] N.I. Kovtyukhova, P.J. Olliver, B.R. Martin, T.E. Mallouk, S.A. Chizhik, E.V. Buzaneva, A.D. Gorchinskiy, Layer-by-Layer assembly of ultrathin composite films from micron-sized graphite oxide sheets and polycations, *Chem. Mater.* 11 (1999) 771–778.
- [24] A.T. Faafarman, W. Koh, B.T. Diroll, D.K. Kim, D. Ko, S.J. Oh, X. Ye, V. Doan-Nguyen, M.R. Crump, D.C. Reifsnnyder, C.B. Murray, C.R. Kagan, Thiocyanate-capped nanocrystal colloids: vibrational reporter of surface chemistry and solution-based route to enhanced coupling in nanocrystal solids, *J. Am. Chem. Soc.* 133 (2011) 15753–15761.
- [25] C. Xu, Y. Liu, J. Wang, H. Geng, H. Qiu, Nanoporous PdCu alloy for formic acid electro-oxidation, *J. Power Sources* 199 (2012) 124–131.
- [26] A.M. Venezia, L.F. Liotta, G. Deganello, Z. Schay, L. Guczi, Characterization of pumice-supported Ag–Pd and Cu–Pd bimetallic catalysts by X-Ray photoelectron spectroscopy and X-Ray diffraction, *J. Catal.* 182 (1999) 449–455.
- [27] J.F. Moulder, W.F. Stickle, P.E. Sobol, K.D. Bomben, *Handbook of X-ray Photoelectron Spectroscopy*, Perkin-Elmer, 1992.
- [28] J. Liu, S. Wang, K. Kravchyk, M. Ibanez, F. Krumeich, R. Widmer, D. Nasiou, M. Meyns, J. Llorca, J. Arbiol, M.V. Kovalenko, A. Cabot, SnP nanocrystals as anode materials for Na-ion batteries, *J. Mater. Chem. A* 6 (2018) 10958–10966.
- [29] V. Tallapally, R.J.A. Esteves, L. Nahar, I.U. Arachchige, Multivariate synthesis of tin phosphide nanoparticles: temperature, time, and ligand control of size, shape, and crystal structure, *Chem. Mater.* 28 (2016) 5406–5414.
- [30] J. Liu, Z. Wang, J. David, J. Llorca, J. Li, X. Yu, A. Shavel, J. Arbiol, M. Meyns, A. Cabot, Colloidal Ni<sub>2-x</sub>Co<sub>x</sub>P nanocrystals for the hydrogen evolution reaction, *J. Mater. Chem. A* 6 (2018) 11453–11462.
- [31] Y. Zhu, S. Murali, W. Cai, X. Li, J.W. Suk, J.R. Potts, R.S. Ruoff, Graphene and graphene oxide: synthesis, properties, and applications, *Adv. Mater.* 22 (2010) 3906–3924.
- [32] L. Chen, L. Lu, H. Zhu, Y. Chen, Y. Huang, Y. Li, L. Wang, Improved ethanol electrooxidation performance by shortening Pd–Ni active site distance in Pd–Ni–P nanocatalysts, *Nat. Commun.* 8 (2017) 14136.
- [33] R.N. Singh, A. Singh, Anindita, Electrocatalytic activity of binary and ternary composite films of Pd, MWCNT and Ni, Part II: methanol electrooxidation in 1M KOH, *Int. J. Hydrogen Energy* 34 (2009) 2052–2057.
- [34] Y. Shen, B. Gong, K. Xiao, L. Wang, In situ assembly of ultrathin PtRh nanowires to graphene nanosheets as highly efficient electrocatalysts for the oxidation of ethanol, *ACS Appl. Mater. Interface* 9 (2017) 3535–3543.
- [35] P. Wang, S. Yin, Y. Wen, Z. Tian, N. Wang, J. Key, S. Wang, P.K. Shen, Ternary Pt9RhFe<sub>x</sub> nanoscale alloys as highly efficient catalysts with enhanced activity and excellent co-poisoning tolerance for ethanol oxidation, *ACS Appl. Mater. Interface* 9 (2017) 9584–9591.
- [36] Q.Q. Xia, L.Y. Zhang, Z.L. Zhao, C.M. Li, Growing platinum-ruthenium-tin ternary alloy nanoparticles on reduced graphene oxide for strong ligand effect toward enhanced ethanol oxidation reaction, *J. Colloid Interface Sci.* 506 (2017) 135–143.
- [37] K. Lee, S.W. Kang, S.U. Lee, K.H. Park, Y.W. Lee, S.W. Han, One-pot synthesis of monodisperse 5 nm Pd–Ni nanoalloys for electrocatalytic ethanol oxidation, *ACS Appl. Mater. Interface* 4 (2012) 4208–4214.
- [38] R. Jana, U. Subbarao, S.C. Peter, Ultrafast synthesis of flower-like ordered Pd<sub>3</sub>Pb nanocrystals with superior electrocatalytic activities towards oxidation of formic acid and ethanol, *J. Power Sources* 301 (2016) 160–169.
- [39] Z. Zhang, S. Liu, X. Tian, J. Wang, P. Xu, F. Xiao, S. Wang, Facile synthesis of N-doped porous carbon encapsulated bimetallic PdCo as a highly active and durable electrocatalyst for oxygen reduction and ethanol oxidation, *J. Mater. Chem. A* 5 (2017) 10876–10884.
- [40] J. Xue, G. Han, W. Ye, Y. Sang, H. Li, P. Guo, X.S. Zhao, Structural regulation of Pd<sub>2</sub>Cu nanoparticles and their electrocatalytic performance for ethanol oxidation, *ACS Appl. Mater. Interface* 8 (2016) 34497–34505.
- [41] Y. Wang, Q. He, J. Guo, J. Wang, Z. Luo, T.D. Shen, K. Ding, A. Khasanov, S. Wei, Z. Guo, Ultrafine FePd nanoalloys decorated multiwalled carbon nanotubes toward enhanced ethanol oxidation reaction, *ACS Appl. Mater. Interface* 7 (2015) 23920–23931.
- [42] T. Liu, K. Wang, Q. Yuan, Z. Shen, Y. Wang, Q. Zhang, X. Wang, Monodispersed sub-5.0 nm PtCu nanoalloys as enhanced bifunctional electrocatalysts for oxygen reduction reaction and ethanol oxidation reaction, *Nanoscale* 9 (2017) 2963–2968.
- [43] C.W. Xu, H. Wang, P.K. Shen, S.P. Jiang, Highly ordered Pd nanowire arrays as effective electrocatalysts for ethanol oxidation in direct alcohol fuel cells, *Adv. Mater.* 19 (2007) 4256–4259.
- [44] A.L. Wang, X.J. He, X.F. Lu, H. Xu, Y.X. Tong, G.R. Li, Palladium–Cobalt nanotube arrays supported on carbon fiber cloth as high-performance flexible electrocatalysts

- for ethanol oxidation, *Angew. Chem. Int. Ed.* 54 (2015) 3669–3673.
- [45] D. Bin, B. Yang, K. Zhang, C. Wang, J. Wang, J. Zhong, Y. Feng, J. Guo, Y. Du, Design of PdAg hollow nanoflowers through galvanic replacement and their application for ethanol electrooxidation, *Chem. Eur. J.* 22 (2016) 16642–16647.
- [46] W. Hong, J. Wang, E. Wang, Facile synthesis of PtCu nanowires with enhanced electrocatalytic activity, *Nano Res.* 8 (2015) 2308–2316.
- [47] K. Jiang, L. Bu, P. Wang, S. Guo, X. Huang, Trimetallic PtSnRh wavy nanowires as efficient nanoelectrocatalysts for alcohol electrooxidation, *ACS Appl. Mater. Interface* 7 (2015) 15061–15067.
- [48] H. Mao, L. Wang, P. Zhu, Q. Xu, Q. Li, Carbon-supported PdSn–SnO<sub>2</sub> catalyst for ethanol electro-oxidation in alkaline media, *Int. J. Hydrogen Energy* 39 (2014) 17583–17588.
- [49] Z.X. Liang, T.S. Zhao, J.B. Xu, L.D. Zhu, Mechanism study of the ethanol oxidation reaction on palladium in alkaline media, *Electrochim. Acta* 54 (2009) 2203–2208.